communications biology

A Nature Portfolio journal

Article

https://doi.org/10.1038/s42003-025-07827-0

Structural and virological identification of neutralizing antibody footprint provides insights into therapeutic antibody design against SARS-CoV-2 variants

Yuki Anraku[1], **Shunsuke Kita**[1]✉, **Taishi Onodera**[2], **Akihiko Sato**[3,4,5], **Takashi Tadokoro**[1], **Shiori Ito**[1], **Yu Adachi**[2], **Ryutaro Kotaki**[2], **Tateki Suzuki**[6], **Jiei Sasaki**[6], **Nozomi Shiwa-Sudo**[7], **Naoko Iwata-Yoshikawa**[7], **Noriyo Nagata**[7], **Souta Kobayashi**[1], **Yasuhiro Kazuki**[8,9], **Mitsuo Oshimura**[10], **Takao Nomura**[1], **Michihito Sasaki**[4,5], **Yasuko Orba**[4,5,11,12], **Tadaki Suzuki**[7], **Hirofumi Sawa**[5,11,12,13], **Takao Hashiguchi**[6,14,15], **Hideo Fukuhara**[1,16], **Yoshimasa Takahashi**[2,5]✉ & **Katsumi Maenaka**[1,5,11,16,17,18]✉

Medical treatments using potent neutralizing SARS-CoV-2 antibodies have achieved remarkable improvements in clinical symptoms, changing the situation for the severity of COVID-19 patients. We previously reported an antibody, NT-108 with potent neutralizing activity. However, the structural and functional basis for the neutralizing activity of NT-108 has not yet been understood. Here, we demonstrated the therapeutic effects of NT-108 in a hamster model and its protective effects at low doses. Furthermore, we determined the cryo-EM structure of NT-108 in complex with SARS-CoV-2 spike. The single-chain Fv construction of NT-108 improved the cryo-EM maps because of the prevention of preferred orientations induced by Fab orientation. The footprints of NT-108 illuminated how escape mutations such as E484K evade from class 2 antibody recognition without ACE2 affinity attenuation. The functional and structural basis for the potent neutralizing activity of NT-108 provides insights into the rational design of therapeutic antibodies.

By 7 March 2025, severe acute respiratory syndrome coronavirus 2 (SARS-CoV-2) had infected 777 million people and caused 7.1 million deaths (https://www.who.int/), and coronavirus disease 2019 (COVID-19) caused by SARS-CoV-2 infection is still ongoing. The most common symptoms of SARS-CoV-2 infection are fever, fatigue, and a dry cough[1,2]. SARS-CoV-2 carries a positive-sense single-stranded RNA[3], and the genome contains two large open reading frames (ORF1a/ORF1b) encoding non-structural proteins (nsp) related to viral replication and transcription, and four ORFs encoding structural proteins: spike (S), envelope (E), membrane (M), and nucleocapsid (N)[4–6].

The spike protein plays an essential role in host cell entry during SARS-CoV-2 infection. The spike protein forms a homotrimer and contains two large domains (S1/S2), which are cleaved at the polybasic sequence (682-RRAR-685) between the S1/S2 domains by serine proteases such as furin during viral maturation[7,8]. The receptor binding domain (RBD) in the spike S1 domain binds to angiotensin-converting enzyme 2 (ACE2) on the host cell surface, and then the S2' site is cleaved by proteases such as transmembrane protease serine 2 (TMPRSS2) to achieve cell entry[9,10]. The activation of the spike protein by cleavage of the S2' site triggers an irreversible conformational change to a post-fusion state, leading to membrane fusion. In addition to such entries, an endosomal pathway independent of the presence of furin and TMPRSS2 is also known[11], and utilizes cathepsin L to activate the spike protein[11,12].

Most neutralizing antibodies can target the spike protein and exhibit neutralizing activity by inhibiting ACE2 binding. Many neutralizing antibodies have been developed as therapeutic and prophylactic treatments for SARS-CoV-2 infection[13–15]. Meanwhile, alpha, beta, delta, and omicron variants lead to outbreaks in many countries because these variants carry amino acid mutations on the spike protein, which results in evasion of the immune response and increased infectivity[16–21]. Therefore, understanding how amino acid mutations can affect the affinity and neutralizing activity of antibodies has important implications for neutralizing antibodies and

A full list of affiliations appears at the end of the paper. ✉e-mail: kita@pharm.hokudai.ac.jp; ytakahas@niid.go.jp; maenaka@pharm.hokudai.ac.jp

vaccine development strategies. Previously, we have reported two neutralizing antibodies, NT-108 and NT-193[22], which were prepared by single-cell sorting technique[23] with the immunization of spike/RBD antigens from SARS-CoV-2, SARS-CoV, and Middle East Respiratory Syndrome (MERS)-CoV to TC-mAb mice, which can stably produce human Ig antibodies[24]. NT-108 was shown to bind to a class 2 epitope[25] and efficiently inhibit ACE2 binding. NT-108 was derived from the IGHV6-1 and IGKV3-20 genes, which are atypical for SARS-CoV-2 neutralizing antibodies[22]. On the other hand, these genes are utilized with a certain frequency in various kind of humanized mice that immunized by SARS-CoV-2 spike antigen[26,27]. Understanding the antigen recognition mechanisms of antibodies can provide insights into strategies to improve the functionality of antibodies and vaccine development. Despite this background, the details of the recognition mechanism of NT-108 have not been clarified.

Here, we focused on determining the SARS-CoV-2 spike protein complexed with NT-108 to understand the recognition mechanism of NT-108. Interestingly, a single-chain Fv (scFv) construct of NT-108 could illuminate the binding mode and details of interaction with RBD residues by addressing the preferred orientation observed in cryo-EM analysis of the spike-NT-108 Fab complex. Cryo-EM structures revealed that NT-108 binds to both the down and up RBDs, and notably, the down RBD bound to NT-108 scFv is in steric contact with the neighboring up RBD, possibly inducing effective inhibition of binding to ACE2. Furthermore, the interaction of the NT-108 H chain with the RBD is assumed to play a pivotal role. The RBD residue E484, which interacts strongly with NT-108 H chain, has emerged as one of the predominant escape mutations in class 2 antibodies[28–30]. Structural insights into the mechanisms by which escape mutations such as E484K affect the antibodies recognition provide a valuable perspective for the development of therapeutic antibodies.

Results

In vivo anti-viral activity of SARS-CoV-2 neutralizing antibody, NT-108

The potent SARS-CoV-2 neutralizing human IgG1 antibody, NT-108, was prepared as described in the same way of our previous report[22] for in vivo prophylactic and therapeutic evaluation. The prophylactic and therapeutic efficacy of NT-108 were examined using a Syrian hamster (Fig. 1), an animal model reproducing mild COVID-19 disease with a short period of weight loss. The hamsters were treated with either 5 mg/kg or 1.25 mg/kg of antibodies at 2 h before (prophylaxis) or 24 h after (therapy) intranasal challenge with SARS-CoV-2 (Fig. 1a). Prophylaxis treatment with NT-108 prevented severe body weight loss in the hamsters until day 6 post-infection (Fig. 1b). The prophylactic effects were more pronounced in the 5 mg/kg group than in the 1.25 mg/kg group, and the effects were evident from the second day after infection. The difference in body weight between the treated and untreated groups continued to widen at later time points. This led to a significant reduction in the viral genome presence in the lungs, particularly in the 5 mg/mL group (Fig. 1c). Similar to the prophylactic treatment, therapeutic treatments prevented body weight loss in hamsters by day 6 after infection, regardless of the dosage (Fig. 1d), although the efficacy was slightly reduced compared to the prophylactic efficacy. The therapeutic effects were also evident by the decreased presence of viral genomes in the lungs (Fig. 1e).

Preparation of the scFv of NT-108 for cryo-EM study

To understand the structural basis of NT-108 recognition for the SARS-CoV-2 spike protein, NT-108 Fab was initially prepared[22] and complexed with SARS-CoV-2 spike 6 P, which was introduced with six proline engineering mutations to stabilize the trimer form for structural analysis by cryo-EM[31]. However, due to the strongly preferred orientation in the grid preparation, the reconstruction of a high-resolution 3D map was not successful, even using the stage-tilt method[32] (Supplementary Fig. 1a–c). Many top views of spike-Fab complexes were observed, suggesting that Fabs strongly interact with the air-water interface. Thus, to address the preferred orientation, the scFv construct was examined instead of the Fab construct of NT-108. Previous studies have reported that the domain orientations[33,34] and flexibilities[35] of single-chain variable fragment (scFv) antibodies, specifically VH-VL or VL-VH orientations, influence their biological activity and productivity. To evaluate which orientation with typical (GGGGS)3 linker exhibits superior properties, two types of scFvs were prepared: one with VH-linker-VL (HL) and the other with VL-linker-VH (LH). Although both constructs showed low refolding efficiency (less than a few percent), the LH scFv for NT-108 showed slightly better inclusion-body yield and refolding efficiency than the HL scFv. According to these results, we decided to use the scFv-LH (VL-VH orientation) for further experiments (Fig. 2a). In addition, we also constructed the mammalian expression vectors for NT-108 scFv, because their expression in *E. coli* was too low to investigate further structural studies. Surface plasmon resonance (SPR) analysis demonstrated the high affinity of both NT-108 scFv prepared in *E. coli* and HEK293T cells to RBD (the K_D values were ~ $10^{-9 \sim -11}$ M), which is comparable to that of its Fab form (Fig. 2b–d).

Cryo-EM structures of NT-108 scFv in complex with spike trimer

Cryo-EM maps of NT-108 scFv and SARS-CoV-2 spike complex were reconstructed at 3.28 Å resolution for both the 1-up and 2-up states (Fig. 3a, Supplementary Fig. 2a–d, Table 1). The low-resolution cryo-EM map for the spike-NT-108 Fab complex showed that NT-108 Fab binds to the down and up RBD in a manner similar to the scFv format (Supplementary Fig. 2e), indicating that the binding mode does not depend on the NT-108 constructs. Both the 1-up and 2-up states showed that NT-108 scFv bound to the down RBD and its neighboring up RBD, possibly locking the conformation of these down and up RBDs. The remaining RBD showed either a down state without NT-108 binding in state 1 or an up state with NT-108 binding in state 2. To clarify the transition between states 1 and 2, superimposing the RBD-NT-108 scFv structure onto the down RBD in state 1 revealed potential clashes with adjacent RBD (Supplementary Fig. 3a). Furthermore, the ratio of particles assigned to state 1 was 35% of all particles assigned to the spike and NT-108 scFv complex (Supplementary Fig. 2b). The state 1 was observed because it represents a potentially stable conformation owing to the interference between the RBD and NT-108 scFv. Further binding of NT-108 scFv was likely to induce a transition to state 2, resulting in a 1:3 binding ratio (spike: NT-108 scFv). The steric conflict occurred at the interface between NT-108 scFv bound to the down RBD and the neighboring up RBD, enforcing the up RBD in a more open conformation than those without antibody or ACE2 binding[36,37] (Fig. 3b). Furthermore, NT-108 VL bound to the down RBD was also in contact with the neighboring up RBD (Supplementary Fig. 3b). These minor contacts between NT-108 and adjacent RBD potentially contributed to the stabilization of the spike and NT-108 complex conformation. Such open conformations have been observed in SARS-CoV-2 spike and antibody complex structures[25,38–43] and may be driven by the inter-domain flexibility of the spike and the high affinity of the antibody, as shown in the SPR analysis in this study (Fig. 2b).

To illuminate the detailed antibody interaction mode, local refinement focused on the down RBD and NT-108 scFv interface was performed, and maps were obtained at 3.27 Å resolution. Neutralizing antibodies against RBD are classified into classes 1 to 4 according to their binding regions in RBD[25]. We have previously shown that NT-108 is an antibody belonging to class 2 in an antibody-competitive assay[22]. Consistent with our previous study, cryo-EM analysis in this study indicated that NT-108 is a class 2 antibody (Fig. 3c). Epitope regions were mapped onto sequences based on RBD-antibody complexes in the Protein Data Bank (PDB), indicating that the recognition sites of NT-108 were similar to those of other class 2 antibodies (Supplementary Fig. 4a). The buried surface area (BSA) of RBD residues was also calculated to assess the contribution of the VH and VL of NT-108 antibodies to RBD recognition (Supplementary Fig. 4b). Interestingly, while most of the class 2 antibodies showed a BSA for VH greater than for VL, NT-108 showed a BSA of 452.4 $Å^2$ for VH and 659.5 $Å^2$ for VL, indicating that the VL of NT-108 more widely recognizes the RBD. Indeed, overlaying the ACE2-interacting residues in the RBD with the NT-108

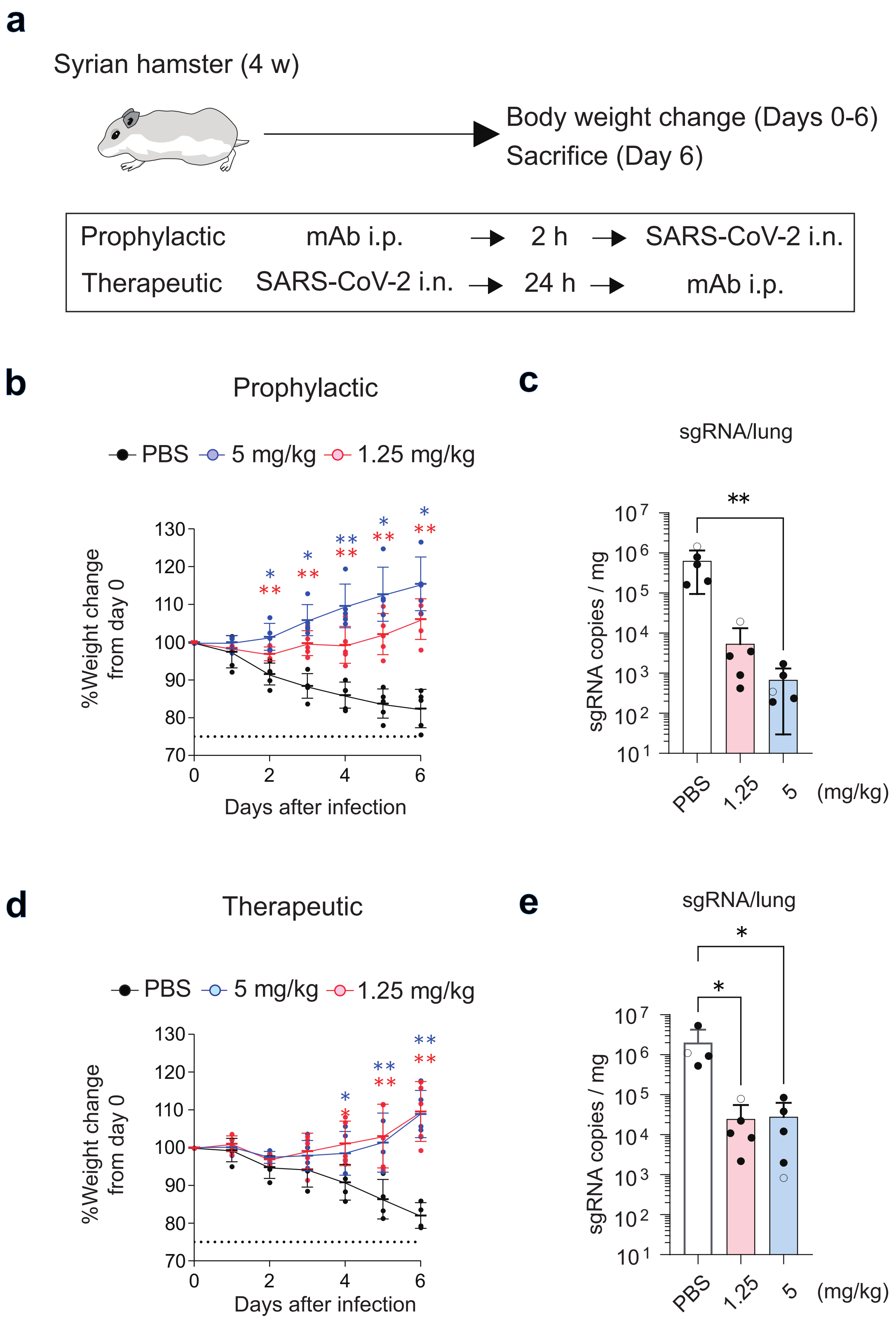

Fig. 1 | Prophylactic and therapeutic effects of NT-108 in a hamster model. **a** Schematic diagram of the experimental design to assess the prophylactic and therapeutic effect of NT-108. i.p., intraperitoneal. i.n., intranasal. **b, d** Body weight of CoV2-challenged hamsters were monitored daily followed by either prophylactic (**b**) or therapeutic (**d**) antibody injection at the indicated doses. Value represents mean ± SD. **c, e** The amounts of CoV-2 viral subgenomic RNA in lung tissues of hamsters receiving either prophylactic (**c**) or therapeutic (**e**) monoclonal antibodies at the indicated doses. Each dot represents the result from an individual animal. Dashed lines indicate the humane endpoint (75% weight change). The combined data from more than two independent experiments ($n = 4$–5 per group) are shown. Statistical analyses were performed using a two-tailed Mann-Whitney test in (**b, d**), Kruskal-Wallis test in (**c, e**). $^*P < 0.05$; $^{**}P < 0.01$.

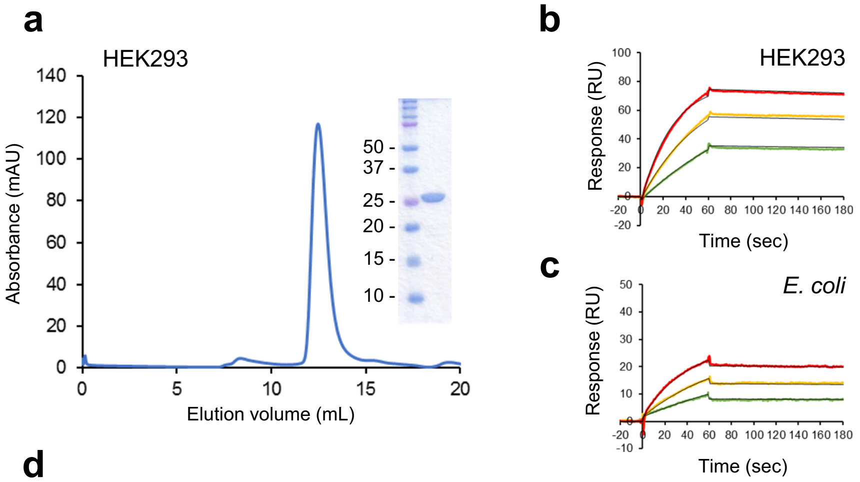

d

Format	Host	K_D (M)	k_{on} (1/Ms)	k_{off} (1/s)
scFv	*E. coli*	2.85×10^{-10}	6.66×10^{5}	1.90×10^{-4}
scFv	HEK293	9.85×10^{-11}	2.94×10^{6}	2.89×10^{-4}
Fab	HEK293	4.52×10^{-10}	6.90×10^{5}	3.13×10^{-4}

Fig. 2 | Biophysical properties of NT-108 scFv. **a** Size exclusion chromatography of NT-108 scFv expression in HEK293 mammalian cells. The results of SDS-PAGE to confirm the purity of the samples are also shown. **b, c** Surface plasmon resonance (SPR) curve for the binding of NT-108 scFv expressed in (**b**) HEK293 and (**c**) *E.coli* to the SARS-CoV-2 RBD. **d**, Kinetic constants for the binding of RBD and NT-108 scFv. The kinetic constants for RBD and NT-108 Fab calculated in our previous study have been described[22].

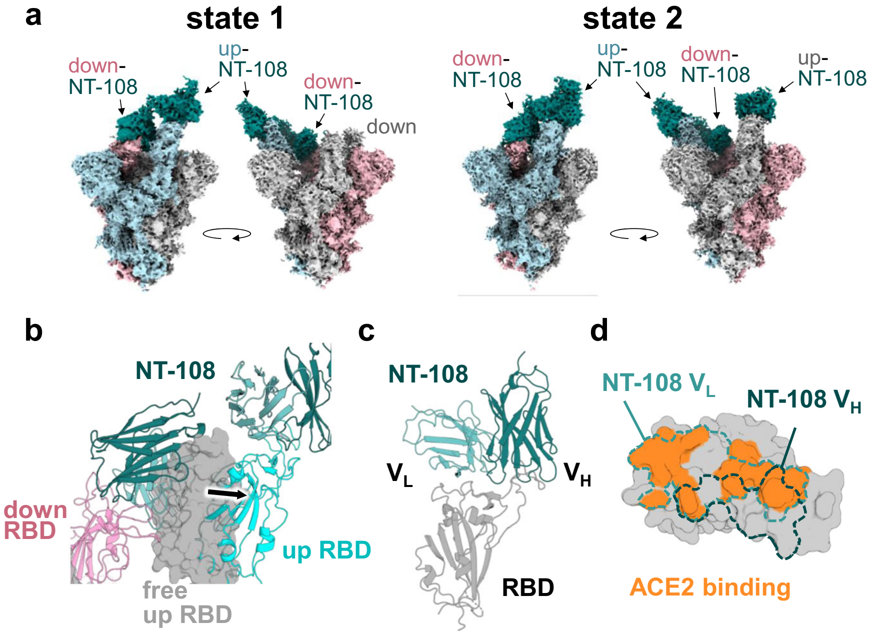

Fig. 3 | Cryo-EM maps of the NT-108 scFv-spike complex shows a class 2 binding mode. **a** Cryo-EM maps of the NT-108 scFv-spike complex showing the two RBD conformations. The cryo-EM maps of each state are shown at two angles. Spike protomers are colored in cyan, pink, and gray. NT-108 scFv is colored deep green. **b** NT-108 scFv bound to the down RBD interferes with the adjacent up RBD. free-up RBD (PDB:6VXX) is shown in the surface representation. **c** The binding mode of NT-108 scFv. **d** Binding sites on the RBD of NT-108 and ACE2-interacting amino acid residues are illustrated; ACE2-interacting amino acid residues are shown in orange and the epitope of NT-108 is circled by dashed lines.

epitope (Fig. 3d) showed that the light chain covered a large area of the ACE2 binding site. We also performed X-ray crystallographic analysis of the RBD complex with the NT-108 Fab. The structure of the complex was determined at a resolution of 2.8 Å (Table 2). The cryo-EM and crystal structures superimposed well, revealing essentially the same interaction mode in both structures (Supplementary Fig. 5a). F486 and Y489 in the RBD are in the vicinity of a hydrophobic environment composed of the aromatic amino acids present at the interface between the heavy and light chains (Fig. 4a). The hydroxy group of Y489 in the RBD interacted with the S114 (IMGT numbering) main chain in CDR-L3 of NT-108, and the S114 side chain in NT-108 interacted with the N487 side chain in the RBD (Fig. 4b). In addition, Y66 of CDR-L2 in NT-108 interacted with Y453 in the RBD (Fig. 4c). In the heavy chain, the main chain atoms of S109 and V110 of CDR-H3 were near the loop containing S494 in the RBD and interacted with the S494 backbone and Q493 side chain in the RBD, respectively (Fig. 4d). Furthermore, R59 in CDR-H2 formed a salt bridge with E484, which cooperated with Y57 in CDR-H2 and Y113 in CDR-H3 to form an interaction network (Fig. 4e).

In ACE2-binding inhibitory activity assays using RBD based on several VOC sequences, NT-108 showed inhibitory activity against Alpha and Delta variants comparable to that of Wuhan-Hu-1 but completely lost inhibitory activity against Beta and Gamma variants (Fig. 4f). Among the amino acid mutations shared by Beta and Gamma, E484K was included in the NT-108 epitope (Fig. 4f, g). To clarify the effect of amino acid mutations on ACE2 binding inhibitory activity, single amino acid mutations, L452R (delta), E484K (beta, gamma), and N501Y (alpha, beta, gamma), were

Table 1 | Cryo-EM data collection, refinement and validation statistics

	SARS-CoV-2 spike – NT-108 scFv complex		
Data collection and processing	**1-up state**	**2-up state**	**RBD and NT-108 interface**
EMDB ID	EMD-39370	EMD-39371	EMD-39372
PDB ID	8YKG	-	8YKH
Microscope	Krios G4		
Camera energy filter	Gatan K3 Gatan Biocontinuum		
slit width	20		
Magnification	130,000		
Recording mode	counting		
Voltage (kV)	300		
Electron exposure (e–/Å^2)	50.4		
Exposure time (s)	1.5		
Number of raw frames	53.52		
Defocus range (μm)	−0.8 to −1.8		
Pixel size (Å)	0.67		
Initial particle images (no.)	652,138		
Final particle images (no.)	84,530	73,060	124,137
Symmetry imposed	C1	C1	C1
Map resolution (Å) FSC 0.143	3.28	3.28	3.27
Refinement			
Initial model used (PDB code)	7K8X	-	8YK4
Model composition			
Protein residues	26426	-	3330
Ligands	NAG:23	-	NAG:2
Map CC	0.80	-	0.84
R.m.s. deviations			
Bond lengths (Å)	0.004	-	0.005
Bond angles (°)	0.563	-	0.631
Validation			
MolProbity score	1.64	-	1.62
Clashscore	6.88	-	5.52
Rotamer outliers (%)	0.00	-	0.00
Ramachandran plot			
Favored (%)	96.19	-	95.44
Allowed (%)	3.81	-	4.56
Outliers (%)	0.00	-	0.00

Table 2 | X-ray data collection and refinement statistics

	SARS-CoV-2 RBD – NT-108 scFv
Data collection	
PDB ID	8YK4
Wavelength (A)	1.00000
Resolution range	48.35–3.20 (3.42–3.20)
Space group	I 2 2 2
Unit cell	55.152 149.641 253.429 90 90 90
Total reflections	166921 (28657)
Unique reflections	17765 (3153)
Multiplicity	9.4 (9.1)
Completeness (%)	99.6 (99.4)
Mean I/sigma(I)	5.7 (1.5)
Wilson B-factor (Å^2)	30.3
R-merge	0.413 (1.819)
R-meas	0.438 (1.934)
R-pim	0.143 (0.645)
CC1/2	0.987 (0.522)
Reflections used in refinement	17737 (1732)
Reflections used for R-free	861 (80)
R-work	0.2433 (0.3235)
R-free	0.2661 (0.3402)
Number of non-hydrogen atoms	3179
macromolecules	3179
Protein residues	408
RMS(bonds)	0.001
RMS(angles)	0.41
Ramachandran favored (%)	93.22
Ramachandran allowed (%)	6.78

introduced into RBDs based on the Wuhan-Hu-1 sequence backbone, and ACE2 binding inhibitory activity was measured by the mesoscale (Fig. 4h). The results showed that neither the L452R nor N501Y single mutation affected the inhibitory activity of NT-108, while the single amino acid mutation, E484K, completely lost the inhibitory activity. E484 formed a salt bridge with R59 of NT-108 CDR-H2 (Fig. 4e). The E484K mutation disrupted the interaction network by losing the salt bridge interaction and inducing repulsion, suggesting that it did not achieve sufficient affinity for ACE2 binding inhibition. To further investigate the importance of the E484 residue in the recognition of the RBD by NT-108, the ACE2 inhibition activity against the E484A and E484Q mutants was tested (Fig. 4h). The inhibition activity against the E484A mutant was stronger than that against the E484K mutant, and it was even stronger against the E484Q mutant. The results supported the idea that the E484 residue is a critical footprint for NT-108 recognition, primarily driven by interactions mediated through salt bridge formation. Subsequently, the ACE2 inhibition activity against Omicron subvariants carrying the E484A mutation (BA.1, BA.2, XBB) and those carrying the E484K mutation (BA.2.86, JN.1, KP.3) was measured (Supplementary Fig. 6). In all tested variants, ACE2 inhibition activity was completely lost. This loss of activity is likely due to the high accumulation and diversification of amino acid mutations in Omicron subvariants at the NT-108 epitope region, in addition to the E484A and E484K mutations.

To further investigate neutralization escape from NT-108, we propagated SARS-CoV-2 in the presence of NT-108 and screened the antibody escape mutant in vitro[22]. Two different single RBD mutations (E484R and S494P) were identified in the escape mutants selected under different antibody concentrations (Fig. 4i). The potential effect of E484R and S494P mutations on viral viability was additionally evaluated using E484R or S494P mutant clones, which were verified to maintain resistance to NT-108 after cloning (Supplementary Fig. 7). The E484R mutation was expected to disrupt the interaction with NT-108, similar to the E484K mutation (Fig. 4e). The S494P mutation in the RBD occurs in the ACE2 interaction site, but the S494 residue does not interact with ACE2[44]. The main chain CDR-H3 loop of NT-108 was near S494 in the RBD, forming a main chain interaction between RBD S494 and NT-108 V110 (Fig. 4d). It is predicted that the S494P mutation breaks the interaction with the main-chain nitrogen atom, resulting in a collision due to more bulkiness of the proline. Thus, both E484K/R and S494P in the RBD blocks the interaction with the heavy chain of NT-108. The heavy chains had a smaller interaction area than that of the light chains (Fig. 3d), these results suggest that heavy chain interactions are important for the strong RBD interactions and potent ACE2 binding inhibitory activity of NT-108.

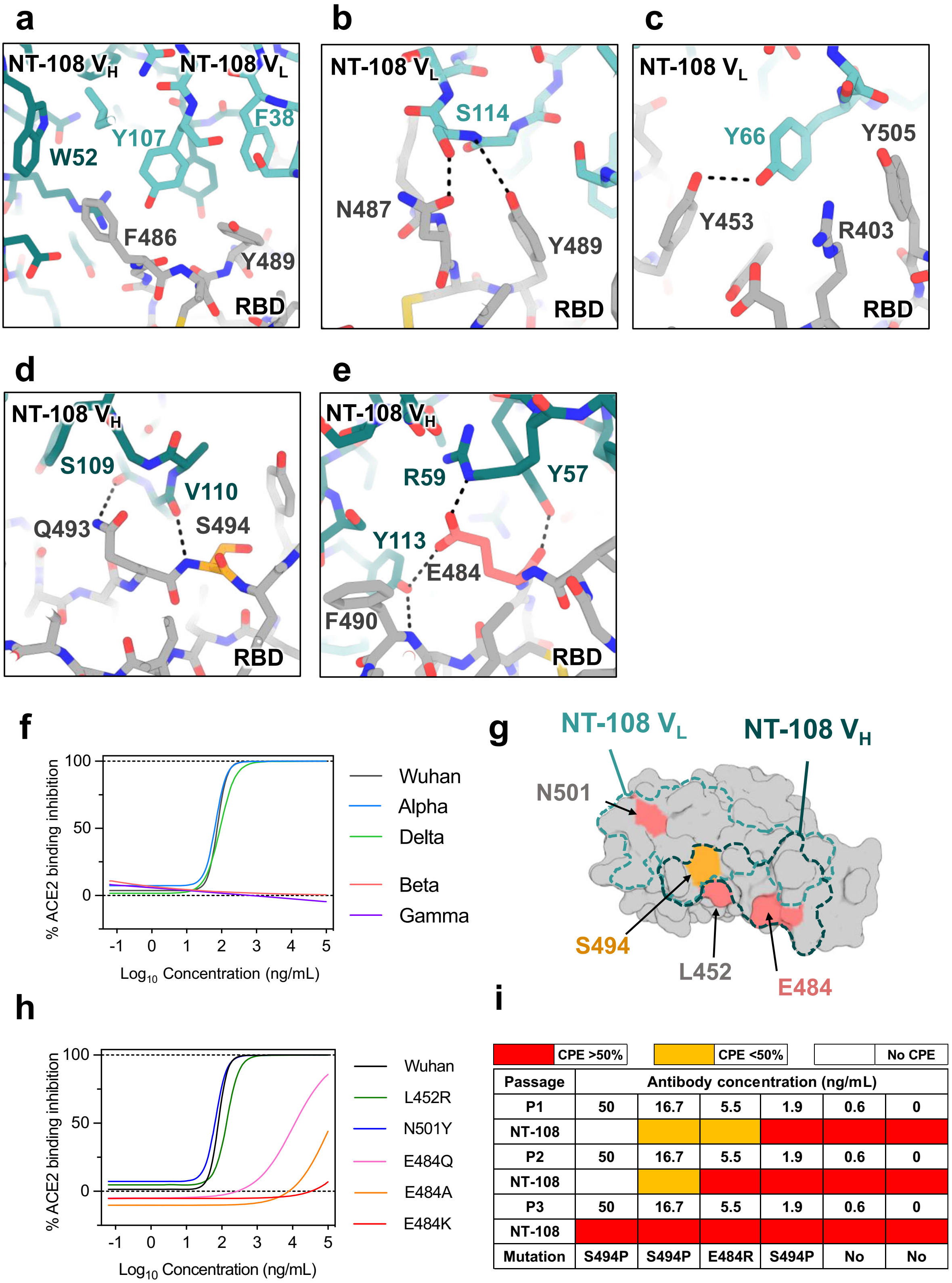

🟥 CPE >50%　🟨 CPE <50%　☐ No CPE

Passage	Antibody concentration (ng/mL)					
P1	50	16.7	5.5	1.9	0.6	0
NT-108		🟨	🟨	🟥	🟥	🟥
P2	50	16.7	5.5	1.9	0.6	0
NT-108		🟨	🟥	🟥	🟥	🟥
P3	50	16.7	5.5	1.9	0.6	0
NT-108	🟥	🟥	🟥	🟥	🟥	🟥
Mutation	S494P	S494P	E484R	S494P	No	No

Discussion

In this study, we provided structural characterization of SARS-CoV-2 neutralizing NT-108 antibody, which was originally derived from RBD-immune humanized mice. NT-108 utilizes the atypical IGHV6-1 gene, according to the Cov-Abdab database[45], there are only 10 reports of IGHV6-1 compared to 585 reports of IGHV3-53, which is known to be highly induced by humans exposed to SARS-CoV-2 antigens[46]. NT-108 also utilizes the IGKV3-20 gene, this pairing (IGHV6-1/IGKV3-20) was shared by five antibodies[19,40,47,48], such as BD-922, BD55-927, and 28C5, which were reported to exhibit neutralizing activity against SARS-CoV-2 WT (Supplementary Table. 1). Furthermore, NT-108 showed potent prophylactic and therapeutic effects in hamster (Fig. 1), an animal model reproducing

Fig. 4 | Structural details of NT-108 scFv-spike explain loss of ACE2 binding inhibition activity and escape mutation. a–e Detailed recognition mode of (**a**) V_H-V_L interface, (**b**) CDR-L3, (**c**) CDR-L2, (**d**) CDR-H3, (**e**) CDR-H2 and CDR-H3 of NT-108. The dotted lines indicate polar interactions. **f** Binding sites on the RBD of NT-108, amino acid mutation sites that are carried by the SARS-CoV-2 variant, and NT-108 escape mutation site are illustrated. The epitope of NT-108 is circled by dashed lines, the variant mutations are pink, and the NT-108 escape mutation is yellow. **f, g** ACE2 binding inhibition activities of NT-108 were examined by mesoscale, and inhibition percentages are plotted. **f** SARS-CoV-2 Wuhan, Alpha, Delta, Beta and Gamma variants (**g**) single amino acid mutation (L452R, N501Y, E484Q, E484A and E484K) in RBD. **h** Binding sites on the RBD of NT-108, amino acid mutation sites that are carried by the SARS-CoV-2 variant, and NT-108 escape mutation site are illustrated. The epitope of NT-108 is circled by dashed lines, the variant mutations are pink, and the NT-108 escape mutation is yellow. **i** Isolation of NT-108- escape mutants of SARS-CoV-2. SARS-CoV-2 was serially passaged in the indicated concentrations of NT-108. At 2 days post-inoculation, cytopathic effect (CPE) was observed under a microscope. The amino acid substitutions in the spike after 3 passages are indicated at the bottom of the table.

mild COVID-19 disease, although the prophylactic and therapeutic effects for severe COVID-19 disease remain tested in other animal models causing lethal infection[49]. Structural analysis of the NT-108 scFv complex with the SARS-CoV-2 spike revealed the binding mode of NT-108, with both the heavy and light chains recognizing most of the ACE2 binding site of the RBD. We also clarified the effects of mutation in VOC and escape mutations on the affinity of NT-108.

The cryo-EM analysis in this study used the scFv construct rather than the Fab construct (Fig. 2), which is generally used for the analysis of spike and neutralizing antibody complexes. The quality of cryo-EM maps of the complex was improved using scFv (Fig. 3); thus, the spike-NT-108 scFv complex illuminated the details of the interaction between RBD and NT-108 (Fig. 4). The stage tilt method and detergents have been used to address orientation bias[32,50], but no significant improvement in cryo-EM map resolvability was observed in the spike-NT-108 Fab complexes (Supplementary Fig. 1). The scFv construction would have the potential to improve the high-resolution features suffered from the preferred orientation in cryo-EM analysis.

The analysis of the buried surface area (BSA) of class 2 antibodies showed that NT-108 recognizes RBD synergistically, involving both VH and VL chains more effectively than other antibodies (Supplementary Fig. 3b). The neutralizing antibodies of the same class 2 as NT-108, which show comparable BSA values (1,111.9 Å^2), show a greater contribution from the VH domain. This pattern is also observed across other classes of neutralizing antibody, where the VH contribution is typically more dominant[25]. For example, antibodies with similar BSA values for NT-108, such as COR-101 (1,132.9 Å^2, class 1), CB6 (1,078.3 Å^2, class 1), and S309 (1,078.3 Å^2, class 3), all exhibit a stronger VH contribution[51–53]. Therefore, the significant contribution of the VL domain in NT-108 is a notable feature, highlighting its high potential in antibody development on interaction site of VH and VL. Indeed, the light chain of NT-108 forms interactions with the Y489 residue of the RBD, which is known to be less prone to amino acid mutations[54–56].

The trapping of the pre-fusion state is one of the factors contributing to the neutralizing activity of antibodies[42]. The pre-fusion trapping is the conformational locking of the spike that inhibits the transition to the post-fusion state, thereby preventing membrane fusion. NT-108, like the 5A6 antibody[42], might fix one of the RBDs in the down state while in contact with the other RBDs in the up state (Fig. 3b). Therefore, the steric NT-108 binding may induce the trapping of the pre-fusion state of the spike protein to inhibit the transition to the post-fusion state. In summary, the cryo-EM analysis of NT-108 suggests that NT-108 clearly competes with ACE2 binding to the spike, leading to potent neutralizing activity, and may exhibit additional effects on inhibitory activity for membrane fusion.

Understanding the binding mode of IgG is critical for considering its neutralization mechanism. An IgG, with two Fab regions linked by a flexible hinge loop through Fc, can achieve bivalent binding. To investigate whether one IgG molecule could simultaneously bind two RBDs of one single spike, we analyzed the IgG binding mode based on the spike and NT-108 scFv complex structure (state 2). The distances between the S494 residues at the center of each NT-108 epitope were measured as 68.7 Å, 90.8 Å, and 57.8 Å (Supplementary Fig. 8). The consideration of VH-CH1 orientation from the scFv binding mode suggests that IgG bound to the most distant RBD (90.8 Å) would likely orient outward from the spike. In contrast, for the two RBDs spaced at 57.8 Å, the VH-CH1 orientation appears feasible for simultaneous binding by IgG. When considering a 1:3 binding stoichiometry, the proximity of the down RBD and the up RBD could lead to potential steric hindrance between IgG molecules, which might prevent the transition from a 1:2 to 1:3 binding stoichiometry. If these two RBDs assume a more open conformation, a 1:3 binding ratio may be allowed. Additionally, to further understand the binding stoichiometries of the spike protein with the NT-108 scFv, Fab, or IgG formats, we performed the preliminary experiment using mass photometry (Two MP, Refeyn) to measure the mass distribution of the complexes. The spike protein was mixed with all three formats of NT-108 in a 1:3 molar ratio and analyzed by mass photometry. The mass distribution shift indicated that, notably, the spike: scFv and spike: Fab complexes were formed in a 1:3 ratio, while the spike: IgG complex formed a 1:2 ratio (Supplementary Fig. 9). While three scFvs or Fabs can bind to all three RBDs of one spike, IgG exhibited a dominant binding complex of two molecules with one spike, suggesting that one of the two IgG molecules occupies the two RBDs because of the high affinity and sufficient concentration of NT-108 IgG. Notably, COVA2-15, another class 2 antibody, showed a similar stoichiometric profile in mass photometry experiments, with 1:3 binding for Fab and 1:2 for IgG, consistent with our results[57].

Several reports have shown that the E484K mutation in the RBD reduced the neutralizing activity of plasma antibodies primed by ancestral vaccines or infection[28–30]. Many class 2 antibodies, including NT-108, interact with E484 (Supplementary Fig. 3a), indicating that the E484K mutation likely affects the antibody affinity. The ACE2 inhibition activity profiles of NT-108 for the E484A and E484Q mutants differed from that of the E484K mutant, suggesting a significant contribution of the specific interactions with the E484 residue in RBD recognition. Furthermore, The RBD E484R mutation was identified in the NT-108 antibody escape mutant (Fig. 4h). In addition, the S494P mutation has been also found in circulating virus sequences like B.1.575 and B.1.623[58,59]. The S494P mutation reportedly leads to evasion of neutralizing antibodies without reduction of ACE2 affinity[60–63]. Importantly, neither the E484 nor S494 residues directly interact with ACE2 residues[44]. These results suggest that such residues are more likely to be observed as mutation sites, because these mutations allow antibody evasion without reducing ACE2 affinity. Considering these findings, neutralizing antibodies that recognize amino acid residues in the RBD that interact with ACE2 or that are less frequently mutated in circulating viral sequences may be expected to have broad neutralizing activity. Indeed, our previous report demonstrated that NIV-10 antibody exhibited broad neutralizing activity and critically recognized RBD Y489, which is strongly associated with ACE2 affinity. Furthermore, NIV-10 has been used as a template for rational antibody development via computational design to restore neutralizing activity to emerging variants[54]. On the other hand, NT-193 antibody, which was also identified in the same experiment as NT-108, recognizes G504 as a key footprint. The G504V mutation was an escape mutation for NT-193 but reduced ACE2 affinity, suggesting that NT-193 could also be a useful template for antibody development[22]. Taken together, structural insights into the neutralizing mechanisms of NT-108 and the impact of amino acid mutations on affinity provide valuable insights into the impact of amino acid mutations and inform strategies for the development of neutralizing antibodies with broad neutralizing activities.

Methods

Monoclonal IgG preparation, expression and purification

The recombinant NT-108 monoclonal IgG1 antibody and Fab, were produced in the same way of the previous reports[23,64,65] as follows. The variable regions of the immunoglobulin heavy and light chains from single-cell cultures were cloned into human IgG1 heavy chain, heavy chain CH1, and kappa light chain expression vectors. The heavy chain and light chain vector pairs were co-expressed using the Expi293 system (Thermo Fisher Scientific). IgG1 was purified with a Protein G column (Thermo Fisher Scientific, 17-0404-01), and the Fab fragment was purified with a Talon column (Clontech, 635504).

Hamster challenge studies

To determine the protective effect of antibody treatment against SARS-CoV-2 infection in a hamster model, female Syrian hamsters of 4 weeks old (Japan SLC) were anesthetized by i.p. injection of ketamine hydrochloride/xylazine and then i.n. infected with the SARS-CoV-2 (hCoV-19/Japan/TY-WK-521/2020) virus at a dose of 10^4 TCID50 in a volume of 80 µl. The antibodies were diluted with PBS at 5 or 1.25 mg/kg of body weight and then administered by i.p. injection either 2 h before viral challenge for prophylactic treatment or 24 h after viral challenge for therapeutic treatment. All hamsters were monitored daily for survival and body weight loss until 6 days after infection. The humane endpoint was set as a weight loss of 25% relative to the initial body weight at the time of the viral challenge (day 0). All hamsters were randomly assigned to individual cages within each experimental group upon arrival at the facility. They were maintained under specific pathogen free (SPF) conditions and used at 4 week of age. The order of the infection procedures and the cage placement in the isolation cabinet was randomized for each experiment. All animal studies were approved from the Institutional Review Board of the National Institute of Infectious Diseases, Japan, and conducted in accordance with the guidelines of the Institutional Animal Care and Use Committee of the National Institute of Infectious Diseases, Japan. We have complied with all relevant ethical regulations for animal use.

Inhibition of ACE2 binding

Spike RBD-ACE2 binding inhibition activity was measured using a V-PLEX SARS-CoV-2 Panel 11 Kit and U-PLEX kits (Meso Scale Discovery, K15458U and K15235N), according to the manufacturer's instructions. Briefly, for the U-PLEX kit, recombinant biotinylated RBDs were immobilized on the plates via the linker protein. V-PLEX plates or RBD-immobilized U-PLEX plates were incubated with MSD Blocker A reagent (Meso Scale Discovery, R93AA) and then incubated with a diluted monoclonal antibody at room temperature for 1 h with rotation. After the incubation, SULFO-TAG Human ACE2 protein (Meso Scale Discovery, D21ADG-3) was added to the plates. Electrochemiluminescence was measured with MSD Gold read buffer B (Meso Scale Discovery, R60AM) and MESOQuickPlex SQ 120 (Meso Scale Discovery). The percentage of inhibition was determined by the positive control signals, where no antibody was added, and the nonlinear regression curve was calculated using Prism 9 (GraphPad).

Selection of antibody escape SARS-CoV-2

The ancestral SARS-CoV-2 strain WK-521 (lineage A, EPI_ISL_408667) was kindly provided by Dr. Saijo (National Institute of Infectious Diseases, Tokyo, Japan). Vero-TMPRSS2 cells [Vero E6 cells (ATCC, CRL-1586) stably expressing human TMPRSS2][66] were maintained in Dulbecco's Modified Eagle's Medium (DMEM) containing 10% FBS. To isolate NT-108-resistant mutants, mixed cell suspensions of SARS-CoV-2-infected and uninfected Vero-TMPRSS2 cells were plated onto 24-well plates and cultured in the presence of different concentrations of NT-108 antibody (50, 16.7, 5.5, 1.9, 0.6, and 0 µg/ml). The cells were suspended and passaged with naïve Vero-TMPRSS2 every 2 days. After 3 passages, the spike genes of the passaged viruses were sequenced.

Preparation of SARS-CoV-2 spike and RBD

The human codon-optimized nucleotide sequence coding for the spike protein of the SARS-CoV-2 isolate (GenBank: MN994467) was synthesized commercially (Eurofins Genomics). The RBD (amino acids: 331–529), along with the signal peptide (amino acids 1–20; MIHSVFLLMFLLTP-TESYVD) plus a histidine tag with/without Avitag, was cloned into the mammalian expression vector pCAGGS. Following mutations were introduced into Wuhan RBD to produce variant RBDs; E484K, E484A, E484Q, 371 F, S375F, T376A, D405N / R408S / K417N / N440K / S477N / T478K / E484A / Q493R / Q498R / N501Y / Y505H for BA.2, G339D / R346T / L368I / S371F / S373P / S375F / T376A / D405N / R408S / K417N / N440K / V445P / G446S / N460K / S477N / T478K / E484A / F486S / F490S / Q498R / N501Y / Y505H for XBB, I332V / G339H / K356T / S371F / S373P / S375F / T376A / R403K / D405N / R408S / K417N / N440K / V445H / G446S / N450D / L452W / N460K / S477N / T478K / N481K / V483del / E484K / F486P / Q498R / N501Y / Y505H for BA.2.86, I332V / G339H / K356T / S371F / S373P / S375F / T376A / R403K / D405N / R408S / K417N / N440K / V445H / G446S / N450D / L452W / L455S / N460K / S477N / T478K / N481K / V483del / E484K / F486P / Q498R / N501Y / Y505H for JN.1, I332V / G339H / K356T / S371F / S373P / S375F / T376A / R403K / D405N / R408S / K417N / N440K / V445H / G446S / N450D / L452W / L455S / F456L / N460K / S477N / T478K / N481K / V483del / E484K / F486P / Q493E / Q498R / N501Y / Y505H for KP.3. Biotinylated BA.1 RBD protein was purchased from ACROBiosystems (SPD-C82E4). A soluble version of the spike protein (amino acids 1–1210), including the C-terminal T4 foldon trimerization domain, and a double strep-tag, was cloned into the *Drosophila* expression vector pMT[18]. The protein sequence was modified to remove the polybasic furin-cleavage site (RRAR to GSAG), and six stabilizing mutations were introduced (F817P, A892P, A899P, A942P, K986P, and V987P; wild-type numbering)[31]. Recombinant proteins were produced using the *Drosophila* expression system, 293S GnTI (-) or Expi293F cells (Thermo Fisher Scientific, A14527). For producing biotynylated RBDs, the RBD expression vector and BirA-Flag plasmid (Addgene, 64395) were co-expressed, and 100 µM biotin (TCI, B0463) was added to biotinylate the RBDs. Supernatants from transfected cells were harvested on day 5 post-transfection and recombinant proteins were purified using cOmplete His-Tag Purification Resin (Roche, 5893682001) or StrepTactin XT 4Flow high capacity (Iba Lifesciences, 25030010). For the spike protein, Superose 6 Increase 10/300 GL size-exclusion chromatography (Cytiva, 29091596) with calcium- and magnesium-free PBS buffer was performed. For the RBD, Superdex 75 Increase 10/300 GL size-exclusion chromatography (Cytiva, 29148721) with calcium- and magnesium-free PBS buffer was performed.

Preparation of single chain variable fragments

For the recombinant protein production using *E. coli* expression system, the expression plasmids encoding NT-108 scFvs with VH-linker-VL (HL) and VL-linker-VH (LH) orientations were constructed in a similar way of the previous report[33] as follows. To construct scFv expression vectors in HL and LH orientation, using splicing overlap extension PCR[67] with a flexible (GGGGS)3 linker. Template cDNAs for variable domains of heavy and light chains in phIgG1-NT108 and phIgk-NT108 vectors were amplified with primers containing linker sequences. The products were used for a second PCR using KOD-Plus DNA polymerase (TOYOBO, KOD-201). The fragments were digested with NdeI (New England Biolabs, R0111L) and HindIII (New England Biolabs, R0104L), ligated into pET22b. The expression plasmid of the scFv introduced into *E. coli* strain Rosetta 2(DE3) (Novagen, 71397). The transformants were cultured in 2×YT medium containing 100 mg/L ampicillin and 30 mg/mL chloramphenicol at 37 °C. When the OD600 reached to 0.5, isopropyl β-d-thiogalactopyranoside (IPTG) was added for induction, at a final concentration of 1 mM and cultured for an additional 4 hours. After induction, the cells were harvested by centrifugation at 5000×g for 10 min. The inclusion bodies of scFv were isolated from the cell pellet by sonication and were washed repeatedly with Triton wash buffer (50 mM Tris-HCl pH 8.0, 100 mM NaCl, 0.5% Triton

X-100). The purified inclusion bodies were solubilized in denaturant buffer (50 mM Tris-HCl pH 8.0, 10 mM EDTA, 6 M guanidine HCl). The solubilized protein solution was slowly diluted by addition of ice-cold refolding buffer (100 mM Tris-HCl, pH 8.0, 2 mM EDTA, 0.4 M L-Arginine, 3.73 mM cystamine, 6.37 mM cysteamine), to a final protein concentration of 1.5 μM. After incubation for 72 h at 4 °C, the refolded protein solution was concentrated using a VIVAFLOW50 system (Sartorius, VF05P4). The concentrated sample was filtered and subjected to size-exclusion chromatography using a Superdex75 10/300 column (Cytiva, 17517401) with gel filtration buffer (20 mM Tris-HCl pH 8.0, 100 mM NaCl). The fractions containing scFv protein were pooled and concentrated to 1.0 mg/mL.

For the recombinant protein production using mammalian expression system, the expression plasmid was constructed by inserting the DNA fragment encoding the scFv (VH-(GGGGS)3-VL or VL-(GGGGS)3-VH) and C-terminal 6x histidine into pCA7 vector[68], that regulated under the chicken beta actin (CAG) promoter. Proteins were secreted into the culture supernatant via an authentic signal sequence at the N-terminus and purified with 6xHis-tag at the C-terminus. Briefly, the plasmid DNA was transfected into HEK293T cells using PEI-max (Polyscience, Inc., 24765) and allowed to remain for a further 3 days. The culture supernatant was filtered and subsequently applied to Ni Sepharose excel resin (Cytiva, 17371201) and eluted with a buffer containing 150 mM imidazole (25 mM Tris-HCl pH 8.0, 150 mM NaCl, 150 mM imidazole). The fractions containing scFvs were pooled and further applied onto the Superdex75 10/300GL column in gel filtration buffer (20 mM Tris-HCl pH 8.0, 100 mM NaCl).

The protein concentration was determined using a UV spectrophotometer U-5100 (HITACHI), and the purity was determined by sodium dodecyl sulfate polyacrylamide gel electrophoresis (SDS-PAGE).

Surface plasmon resonance (SPR)

The scFv of NT-108 was dissolved in HBS-EP buffer (10 mM HEPES pH7.4, 150 mM NaCl, 3 mM EDTA, 0.005% Surfactant P20). SPR experiments were performed using Biacore3000 (Cytiva). Streptavidin was immobilized on the sensor chip CAP by the standard biotin capture kit, followed by the biotinylated S-RBD (100 to 500 RU). The biotinylated β2-microglobulin was used as a negative control protein. scFv was injected over the immobilized S-RBD protein at a flow rate of 30 μL/min. Flow cells were regenerated with 10 mM glycine (pH 1.5). The data were analyzed using BIA evaluation software version 4.1.1.

Crystallization, data collection, and structural determination

Purified SARS-CoV-2 RBD and NT-108 scFv were mixed at a molar ratio of 1:1.3, followed by purification of the RBD-scFv complex by superdex200 10/300 equilibrated with 20 mM Tris pH8.0, 100 mM NaCl. The fraction containing both RBD and scFv were collected and concentrated until 7.3 mg/mL. Crystallization screening was performed by crystallization robot mosquito using commercially available screening kits. Crystals of RBD-scFv complex were grown at 20 °C by the sitting drop vapor-diffusion method. The final crystallization condition was 0.1 M CHES pH9.5, 20% PEG8000.

The crystals were cryo-cooled in liquid nitrogen and the X-ray diffraction experiments were performed at beamline BL32XU of SPring-8 (Harima, Japan). The X-ray diffraction dataset was processed with XDS and scaled with Aimless in the CCP4 program package[69–71]. The structure was solved by the molecular replacement method using the Phaser program in the PHENIX package. The RBD structure[72] (PDB: 6W41) and the NT-108 scFv fragment which was generated with alphafold2 colab website[73] were used as search probes for molecular replacement. The structure refinement was carried out using phenix.refine and COOT[74,75]. The stereochemical properties of the structures were assessed using MolProbity[76].

Cryo-EM sample preparation and data collection

To prepare a complex sample for cryo-EM, purified NT-108 scFv or Fab were incubated with SARS-CoV-2 spike at a molar ratio of 1 : 2 at 18 °C for 1 h. A 0.02% (w/v) Hexadecyltrimethylammonium bromide (CTAB) solution (Jena Bioscience, X-CEM-301) was added to spike/NT-108 Fab solution to a final concentration of 0.005%. The sample was applied to Quantifoil R1.2/1.3 Cu 300 mesh grid (Quantifoil Micro Tools GmbH), which had been freshly glow-discharged for 90 s at 10 mA using PIB-10 (Vacuum Device). The sample was plunged into liquid ethane using Vitrobot Mark IV (Thermo Fisher Scientific). The settings were as follows: Temperature set to 18 °C, Humidity at 100%, Blotting time is 5 s, Blotting force set to 5.

Movies were collected on a Krios G4 (Thermo Fisher Scientific) operated at 300 kV with a K3 direct electron detector (Gatan) at a nominal magnification of 130,000 (0.67 per physical pixel) using a GIF-Biocontinuum energy filter (Gatan) with a 20 eV slit width. For spike and NT-108 scFv complex, a total of 2832 movies for NT-108 scFv complex were collected. For spike and NT-108 Fab complex, 1062 movies (0° tilt) and 1338 (30° tilt) were collected. All movies were collected with a total exposure 1.5 s and a total dose of 53.52 e/Å^2 over 50 frames at a nominal defocus range of 0.8–1.8 μm using EPU.

Cryo-EM Image processing and model refinement

For spike and NT-108 scFv complex, the movie frames were aligned and dose-weighted using MotionCor2[77]. The contrast transfer function estimation was performed using CTFFIND4[78], and 2081 micrographs were selected. A total of 652,138 particles were auto-picked by crYOLO[79] using a general model, and two rounds of 3D classification (K = 4, T = 4 or 8) using the cryo-EM map of the SARS-CoV-2 spike closed state as a reference map were performed in RELION3.1[80] to remove junk particles. To address the flexibility of the RBD region, the particles were aligned by 3D refinement, followed by 3D classification without alignment focused on the RBD. Two representative states, the 1-up state and 2-up state were reconstructed, then CTF refinement and Bayesian Polishing were performed, and both maps of the 1-up state and 2-up state achieved a resolution at 2.86 Å. To illustrate the NT-108 scFv binding mode, 3D classification without alignment focused on the down RBD and NT-108 scFv interface was performed for the particles with 1-up and 2-up states, and the classes that clearly showed NT-108 scFv binding were selected. Finally, the particles were imported to cryoSPARC v3.3.1[81] and a local map at 3.27 Å resolution was reconstructed by local refinement.

For spike and NT-108 Fab complex, the datasets were processed using RELION3.1. The movie frames were aligned, dose-weighted, and CTF-estimated using MotionCor2 correction and CTFFIND4. To make templates for particle picking, Laplacian of Gaussian picking and 2D classification was performed. 574,809 particles from 0° tilt micrographs and 727,990 particles from 30° tilt micrographs were separately picked by template-picking followed by 2D classifications were performed to remove the junk particles. To reconstruct the initial model, 3D classification with the particles from the dataset of 30° tilt using cryo-EM map of the SARS-CoV-2 spike closed state as reference model was performed. All particles were used for 3D classification. The final map was reconstructed by CTF refinement, Bayesian polishing and 3D refinement. The details of the workflow for cryo-EM data processing are shown in (Supplementary Figs. 1b, 2b). The reported resolutions were based on the gold-standard Fourier shell correlation curves (FSC = 0.143) through RELION3.1. Local resolution was estimated using the RELION implementation program (Supplementary Fig. 2c).

For model refinement, structures of SARS-CoV-2 spike in complex with C121[25] (PDB: 7K8X) and the crystal structure of RBD and NT-108 scFv complex described above were fitted to the corresponding maps using UCSF Chimera v1.14[82]. Iterative rounds of manual fitting in COOT v0.9.8[74] and real-space refinement in Phenix v1.18[75] were carried out to improve the non-ideal rotamers, bond angles, and Ramachandran outliers. The final model was validated with MolProbity[76]. The structure models and cryo-EM maps shown in figures were prepared with The PyMOL Molecular Graphics System, Version 2.3.3 Schrödinger, LLC, UCSF Chimera v1.1.4[82] and UCSF ChimeraX v1.4[83]. The model fitted to the corresponding maps is shown in (Supplementary Fig. 4b). Intermolecular contact atoms were analyzed using PISA and CONTACT in the CCP4 program package[84].

Statistics and reproducibility

All statistical analyses were conducted using GraphPad Prism. The specific tests are detailed in the Methods section and figure legends. In brief, the Mann-Whitney test was used for body weight data (Fig. 1b, d) and Kruskal-Wallis test for viral RNA quantification (Fig. 1c, e). Statistical significance was set at $p < 0.05$. Hamster challenge studies were repeated twice, with 4–5 animals per group (total of 29 animals). Syrian hamsters (1 month old) were randomly assigned to groups. Sample sizes were determined based on prior studies and ethical guidelines to minimize animal use, while ensuring statistical power. Experiments on neutralizing activity (Supplementary Fig. 7) used three independent samples with data from two experiments. Data are presented as the mean ± SD. For protein purification, biophysical and biochemical assays, recombinant protein concentrations were measured by UV absorbance at 280 nm, and purity was assessed by SDS-PAGE and size-exclusion chromatography. Structural analysis was performed using X-ray crystallography and cryo-electron microscopy, and the statistics and metrics are summarized in Tables 1 and 2.

Reporting summary

Further information on research design is available in the Nature Portfolio Reporting Summary linked to this article.

Data availability

The atomic coordinates and cryo-EM maps for the structures of the SARS-CoV-2 spike protein in complex with NT-108 scFv state 1 (8YKG, EMD-39370), state 2 (EMD-39371), and the structure of RBD and NT-108 scFv interface (8YKH, EMD-39370) are available in the Protein Data Bank (www.rcsb.org) and Electron Microscopy Data Bank (www.ebi.ac.uk/emdb/). The atomic coordinates and structure factors of the crystal structure of RBD and NT-108 scFv complex (8YK4) are also available in the Protein Data Bank. Sequences data for NT-108 have been deposited in GenBank under following accession numbers (MW619740 and MW619741). All other data are available in the main text or the supplementary materials. The source data behind the graphs in the paper can be found in Supplementary Data 1.

Received: 3 April 2024; Accepted: 26 February 2025;

References

1. Huang, C. et al. Clinical features of patients infected with 2019 novel coronavirus in Wuhan, China. *Lancet* **395**, 497–506 (2020).
2. Chen, N. et al. Epidemiological and clinical characteristics of 99 cases of 2019 novel coronavirus pneumonia in Wuhan, China: a descriptive study. *Lancet* **395**, 507–513 (2020).
3. Hu, B., Guo, H., Zhou, P. & Shi, Z. L. Characteristics of SARS-CoV-2 and COVID-19. *Nat. Rev. Microbiol.* **19**, 141–154 (2021).
4. Gorbalenya, A. E., Enjuanes, L., Ziebuhr, J. & Snijder, E. J. Nidovirales: Evolving the largest RNA virus genome. *Virus Res*. **117**, 17–37 (2006).
5. Zhu, N. et al. A Novel Coronavirus from Patients with Pneumonia in China, 2019. *N. Engl. J. Med.* **382**, 727–733 (2020).
6. Zhou, P. et al. A pneumonia outbreak associated with a new coronavirus of probable bat origin. *Nature* **579**, 270–273 (2020).
7. V'kovski, P., Kratzel, A., Steiner, S., Stalder, H. & Thiel, V. Coronavirus biology and replication: implications for SARS-CoV-2. *Nat. Rev. Microbiol.* **19**, 155–170 (2020).
8. Takeda, M. Proteolytic activation of SARS-CoV-2 spike protein. *Microbiol. Immunol.* **66**, 15–23 (2022).
9. Hoffmann, M. et al. SARS-CoV-2 Cell Entry Depends on ACE2 and TMPRSS2 and Is Blocked by a Clinically Proven Protease Inhibitor. *Cell* **181**, 271–280.e8 (2020).
10. Matsuyama, S. et al. Enhanced isolation of SARS-CoV-2 by TMPRSS2- expressing cells. *Proc. Natl. Acad. Sci. Usa.* **117**, 7001–7003 (2020).
11. Ou, X. et al. Characterization of spike glycoprotein of SARS-CoV-2 on virus entry and its immune cross-reactivity with SARS-CoV. *Nat. Commun*. **11**, 1620 (2020).
12. Daniloski, Z. et al. Identification of Required Host Factors for SARS-CoV-2 Infection in Human Cells. *Cell* **184**, 92–105.e16 (2021).
13. Pinto, D. et al. Cross-neutralization of SARS-CoV-2 by a human monoclonal SARS-CoV antibody. *Nature* **583**, 290–295 (2020).
14. Hansen, J. et al. Studies in humanized mice and convalescent humans yield a SARS-CoV-2 antibody cocktail. *Science (80-)* **369**, 1010–1014 (2020).
15. Westendorf, K. et al. LY-CoV1404 (bebtelovimab) potently neutralizes SARS-CoV-2 variants. *Cell Rep*. **39**, 110812 (2022).
16. Cao, Y. et al. Omicron escapes the majority of existing SARS-CoV-2 neutralizing antibodies. *Nature* **602**, 657–663 (2022).
17. Iketani, S. et al. Antibody evasion properties of SARS-CoV-2 Omicron sublineages. *Nature* **604**, 553–556 (2022).
18. Saito, A. et al. Virological characteristics of the SARS-CoV-2 Omicron BA.2.75 variant. *Cell Host Microbe* 1–16 https://doi.org/10.1016/j.chom.2022.10.003 (2022).
19. Cao, Y. et al. BA.2.12.1, BA.4 and BA.5 escape antibodies elicited by Omicron infection. *Nature* **608**, 593–602 (2022).
20. Li, R. et al. Conformational flexibility in neutralization of SARS-CoV-2 by naturally elicited anti-SARS-CoV-2 antibodies. *Commun. Biol.* **5**, 1–15 (2022).
21. Abassi, L. et al. Evaluation of the Neutralizing Antibody STE90-C11 against SARS-CoV-2 Delta Infection and Its Recognition of Other Variants of Concerns. *Viruses* **15**, 2153 (2023).
22. Onodera, T. et al. A SARS-CoV-2 antibody broadly neutralizes SARS-related coronaviruses and variants by coordinated recognition of a virus-vulnerable site. *Immunity* **54**, 2385–2398.e10 (2021).
23. Adachi, Y. et al. Exposure of an occluded hemagglutinin epitope drives selection of a class of cross-protective influenza antibodies. *Nat. Commun.* **10**, 1–7 (2019).
24. Satofuka, H. et al. Efficient human-like antibody repertoire and hybridoma production in trans-chromosomic mice carrying megabase-sized human immunoglobulin loci. *Nat. Commun.* **13**, 1–15 (2022).
25. Barnes, C. O. et al. SARS-CoV-2 neutralizing antibody structures inform therapeutic strategies. *Nature* **588**, 682–687 (2020).
26. Yang, X. et al. Discovery and characterization of SARS-CoV-2 reactive and neutralizing antibodies from humanized CAMouseHG mice through rapid hybridoma screening and high-throughput single-cell V(D)J sequencing. *Front. Immunol.* **13**, 1–13 (2022).
27. Wang, C. et al. A conserved immunogenic and vulnerable site on the coronavirus spike protein delineated by cross-reactive monoclonal antibodies. *Nat. Commun.* **12**, 1–15 (2021).
28. Moriyama, S. et al. Temporal maturation of neutralizing antibodies in COVID-19 convalescent individuals improves potency and breadth to circulating SARS-CoV-2 variants. *Immunity* **54**, 1841–1852.e4 (2021).
29. Chen, R. E. et al. Resistance of SARS-CoV-2 variants to neutralization by monoclonal and serum-derived polyclonal antibodies. *Nat. Med*. **27**, 717–726 (2021).
30. Wang, P. et al. Antibody resistance of SARS-CoV-2 variants B.1.351 and B.1.1.7. *Nature* **593**, 130–135 (2021).
31. Hsieh, C. et al. Structure-based design of prefusion-stabilized SARS-CoV-2 spikes. *Science (80-)* **369**, 1501–1505 (2020).
32. Zi Tan, Y. et al. Addressing preferred specimen orientation in single-particle cryo-EMthrough tilting. *Nat. Methods* **14**, 793–796 (2017).
33. Tadokoro, T. et al. Biophysical characterization and single-chain Fv construction of a neutralizing antibody to measles virus. *FEBS J* **287**, 145–159 (2020).
34. Bühler, P. et al. Influence of structural variations on biological activity of anti-PSMA scFv and immunotoxins targeting prostate cancer. *Anticancer Res*. **30**, 3373–3379 (2010).

35. Bertoglio, F. et al. SARS-CoV-2 neutralizing human recombinant antibodies selected from pre-pandemic healthy donors binding at RBD-ACE2 interface. *Nat. Commun.* **12**, 1–15 (2021).
36. Benton, D. J. et al. Receptor binding and priming of the spike protein of SARS-CoV-2 for membrane fusion. *Nature* **588**, 327–330 (2020).
37. Wrapp, D. et al. Cryo-EM structure of the 2019-nCoV spike in the prefusion conformation. *Science (80-)* **367**, 1260–1263 (2020).
38. Yao, H. et al. Rational development of a human antibody cocktail that deploys multiple functions to confer Pan-SARS-CoVs protection. *Cell Res*. **31**, 25–36 (2021).
39. Bracken, C. J. et al. Bi-paratopic and multivalent VH domains block ACE2 binding and neutralize SARS-CoV-2. *Nat. Chem. Biol.* **17**, 113–121 (2021).
40. Scheid, J. F. et al. B cell genomics behind cross-neutralization of SARS-CoV-2 variants and SARS-CoV. *Cell* **184**, 3205–3221.e24 (2021).
41. Miersch, S. et al. Tetravalent SARS-CoV-2 Neutralizing Antibodies Show Enhanced Potency and Resistance to Escape Mutations. *J. Mol. Biol.* **433**, 167177 (2021).
42. Asarnow, D. et al. Structural insight into SARS-CoV-2 neutralizing antibodies and modulation of syncytia. *Cell* **184**, 3192–3204.e16 (2021).
43. Piccoli, L. et al. Mapping Neutralizing and Immunodominant Sites on the SARS-CoV-2 Spike Receptor-Binding Domain by Structure-Guided High-Resolution Serology. *Cell* **183**, 1024–1042.e21 (2020).
44. Lan, J. et al. Structure of the SARS-CoV-2 spike receptor-binding domain bound to the ACE2 receptor. *Nature* **581**, 215–220 (2020).
45. Raybould, M. I. J., Kovaltsuk, A., Marks, C. & Deane, C. M. CoV-AbDab: The coronavirus antibody database. *Bioinformatics* **37**, 734–735 (2021).
46. Zhang, Q. et al. Potent and protective IGHV3-53/3-66 public antibodies and their shared escape mutant on the spike of SARS-CoV-2. *Nat. Commun.* **12**, 1–12 (2021).
47. Cao, Y. et al. Imprinted SARS-CoV-2 humoral immunity induces convergent Omicron RBD evolution. *Nature* **614**, 521–529 (2023).
48. Zhou, X. et al. Diverse immunoglobulin gene usage and convergent epitope targeting in neutralizing antibody responses to SARS-CoV-2. *Cell Rep*. **35**, 109109 (2021).
49. Oladunni, F. S. et al. Lethality of SARS-CoV-2 infection in K18 human angiotensin-converting enzyme 2 transgenic mice. *Nat. Commun*. **11**, 6122 (2020).
50. Drulyte, I. et al. Approaches to altering particle distributions in cryo-electron microscopy sample preparation. *Acta Crystallogr. Sect. D Struct. Biol.* **74**, 560–571 (2018).
51. Bertoglio, F. et al. A SARS-CoV-2 neutralizing antibody selected from COVID-19 patients binds to the ACE2-RBD interface and is tolerant to most known RBD mutations. *Cell Rep*. **36**, 109433 (2021).
52. Shi, R. et al. A human neutralizing antibody targets the receptor-binding site of SARS-CoV-2. *Nature* **584**, 120–124 (2020).
53. Huo, J. et al. Neutralization of SARS-CoV-2 by Destruction of the Prefusion Spike. *Cell Host Microbe* **28**, 445–454.e6 (2020).
54. Moriyama, S. et al. Structural delineation and computational design of SARS-CoV-2-neutralizing antibodies against Omicron subvariants. *Nat. Commun.* **14**, 1–17 (2023).
55. Ozawa, T. et al. Rational in silico design identifies two mutations that restore UT28K SARS-CoV-2 monoclonal antibody activity against Omicron BA.1. *Structure* **32**, 263–272.e7 (2024).
56. Shanker, V. R., Bruun, T. U. J., Hie, B. L. & Kim, P. S. Unsupervised evolution of protein and antibody complexes with a structure-informed language model. *Science (80-)* **385**, 46–53 (2024).
57. Yin, V. et al. Probing Affinity, Avidity, Anticooperativity, and Competition in Antibody and Receptor Binding to the SARS-CoV-2 Spike by Single Particle Mass Analyses. *ACS Cent. Sci.* **7**, 1863–1873 (2021).
58. Trobajo-Sanmartín, C. et al. Emergence of sars-cov-2 variant b.1.575.2, containing the e484k mutation in the spike protein, in pamplona, spain, may to june 2021. *J. Clin. Microbiol*. **59**, e0173621 (2021).
59. Gangavarapu, K. et al. Outbreak.info genomic reports: scalable and dynamic surveillance of SARS-CoV-2 variants and mutations. *Nat. Methods* **20**, 512–522 (2023).
60. Lusvarghi, S. et al. Key Substitutions in the Spike Protein of SARS-CoV-2 Variants Can Predict Resistance to Monoclonal Antibodies, but Other Substitutions Can Modify the Effects. *J. Virol*. **96**, e0111021 (2022).
61. Alenquer, M. et al. Signatures in SARS-CoV-2 spike protein conferring escape to neutralizing antibodies. *PLoS Pathog* **17**, 1–25 (2021).
62. Greaney, A. J. et al. Comprehensive mapping of mutations in the SARS-CoV-2 receptor-binding domain that affect recognition by polyclonal human plasma antibodies. *Cell Host Microbe* **29**, 463–476.e6 (2021).
63. Starr, T. N. et al. Deep Mutational Scanning of SARS-CoV-2 Receptor Binding Domain Reveals Constraints on Folding and ACE2 Binding. *Cell* **182**, 1295–1310.e20 (2020).
64. Tiller, T. et al. Efficient generation of monoclonal antibodies from single human B cells by single cell RT-PCR and expression vector cloning. *J. Immunol. Methods* **329**, 112–124 (2008).
65. Schmidt, A. G. et al. Preconfiguration of the antigen-binding site during affinity maturation of a broadly neutralizing influenza virus antibody. *Proc. Natl. Acad. Sci.* **110**, 264–269 (2013).
66. Sasaki, M. et al. SARS-CoV-2 variants with mutations at the S1/ S2 cleavage site are generated in vitro during propagation in TMPRSS2-deficient cells. *PLoS Pathog* **17**, 1–17 (2021).
67. Horton, R. M., Cai, Z. L., Ho, S. N. & Pease, L. R. Gene splicing by overlap extension: tailor-made genes using the polymerase chain reaction. *Biotechniques* **8**, 528–535 (1990).
68. Hitoshi, N., Ken-ichi, Y. & Jun-ichi, M. Efficient selection for high-expression transfectants with a novel eukaryotic vector. *Gene* **108**, 193–199 (1991).
69. Evans, P. Scaling and assessment of data quality. *Acta Crystallogr. Sect. D Biol. Crystallogr.* **62**, 72–82 (2006).
70. Kabsch, W. Integration, scaling, space-group assignment and post-refinement. *Acta Crystallogr. Sect. D Biol. Crystallogr.* **66**, 133–144 (2010).
71. Winn, M. D. et al. Overview of the CCP4 suite and current developments. *Acta Crystallogr. Sect. D Biol. Crystallogr.* **67**, 235–242 (2011).
72. Yuan, M. et al. A highly conserved cryptic epitope in the receptor binding domains of SARS-CoV-2 and SARS-CoV. *Science (80-)* **368**, 630–633 (2020).
73. Mirdita, M. et al. ColabFold: making protein folding accessible to all. *Nat. Methods* **19**, 679–682 (2022).
74. Emsley, P., Lohkamp, B., Scott, W. G. & Cowtan, K. Features and development of Coot. *Acta Crystallogr. Sect. D Biol. Crystallogr.* **66**, 486–501 (2010).
75. Liebschner, D. et al. Macromolecular structure determination using X-rays, neutrons and electrons: Recent developments in Phenix. *Acta Crystallogr. Sect. D Struct. Biol.* **75**, 861–877 (2019).
76. Williams, C. J. et al. MolProbity: More and better reference data for improved all-atom structure validation. *Protein Sci* **27**, 293–315 (2018).
77. Zheng, S. Q. et al. MotionCor2: Anisotropic correction of beam-induced motion for improved cryo-electron microscopy. *Nat. Methods* **14**, 331–332 (2017).
78. Rohou, A. & Grigorieff, N. CTFFIND4: Fast and accurate defocus estimation from electron micrographs. *J. Struct. Biol.* **192**, 216–221 (2015).
79. Wagner, T. et al. SPHIRE-crYOLO is a fast and accurate fully automated particle picker for cryo-EM. *Commun. Biol.* **2**, 1–13 (2019).

80. Zivanov, J. et al. New tools for automated high-resolution cryo-EM structure determination in RELION-3. *Elife* **7**, 1–22 (2018).
81. Punjani, A., Rubinstein, J. L., Fleet, D. J. & Brubaker, M. A. CryoSPARC: Algorithms for rapid unsupervised cryo-EM structure determination. *Nat. Methods* **14**, 290–296 (2017).
82. Pettersen, E. F. et al. UCSF Chimera - A visualization system for exploratory research and analysis. *J. Comput. Chem.* **25**, 1605–1612 (2004).
83. Goddard, T. D. et al. UCSF ChimeraX: Meeting modern challenges in visualization and analysis. *Protein Sci* **27**, 14–25 (2018).
84. Krissinel, E. & Henrick, K. Inference of Macromolecular Assemblies from Crystalline State. *J. Mol. Biol.* **372**, 774–797 (2007).

Acknowledgements

We thank Cong Tian, Satoko Saka, and Sayaka Niizuma at Laboratory of Biomolecular Science, and Center for Research and Education on Drug Discovery, Faculty of Pharmaceutical Sciences, Hokkaido University for technical support. We thank Kazuma Ariga, and Ryoko Itami at National Institute of Infectious Diseases (NIID) for technical support. We thank all members of the Japanese Consortium on Structural Virology (JX-Vir). This study was supported in part by Japan Agency for Medical Research and Development (AMED) [JP17am0101093 (K.M.)]; AMED [JP20ae0101047 (K.M.)]; AMED [JP21fk0108463 (K.M.)]; AMED [JP22ama121037 (K.M.)]; AMED [JP 22gm1810004 (YT and KM)]; AMED [JP23ama121046 (Y.K.)]; Hokkaido University Biosurface project (K.M.); The Scientific Research on Innovative Areas and International Group from the MEXT/JSPS KAKENHI [JP20H05873 (K.M.)] and a Grant-in-Aid for Transformative Research Areas (A) "Latent Chemical Space" [JP23H04880 and JP23H04881 (T.N.)]; Takeda Science Foundation (K.M.); AMED SCARDA Kyoto University Immunomonitoring Center (KIC) [JP223fa627009 (T.H.)]; AMED SCARDA Hokkaido University Institute for Vaccine Research and Development (HU-IVReD) [JP223fa627005 (K.M.), (Y.T.), (M.S.), (A.S.), (O.Y.), (H.S.)]; AMED ASPIRE [JP23jf0126002 (T.H.)]; JST CREST [JPMJCR20H8 (T.H.)]; JSPS Core-to-Core Program (A. Advanced Research Networks) (T.H.); The Cooperative Research Program (Joint Usage/Research Center program) of Institute for Life and Medical Sciences, Kyoto University (K.M.).

Author contributions

Tateki Suzuki., J.S., T.H. produced and purified recombinant proteins. T.O., Y.Adachi., R.K., Y.T., N.S., N.I., N.N. and Tadaki Suzuki. performed in vivo assays and ACE2-binding inhibitory activity assays. Y.K. and M.O. provided TC-mAb model mice. A.S., M.S., Y.O., H.S. performed selection of NT-108 antibody escape SARS-CoV-2. Y.Anraku, S.Kita, T.T., S.I., H.F., K.M. performed the structural studies and analyzed the structural data. T.T. and T.N. prepared and purified recombinant NT-108 scFv and T.T., T.N., S.Kita, and S. Kobayashi performed the binding analysis. T.H., Y.T., Tadaki Suzuki, H.S., K.M. administered the project. Y.T. and K.M. supervised the study. Y.Anraku and K.M. wrote original draft. Y.Anraku, T.H., Y.T., T.S., A.S., S.Kita, T.T. and K.M. reviewed and edited the manuscript.

Competing interests

A.S. is an employee of Shionogi & Co., Ltd. M.O. is a CEO, employee, and shareholder of Trans Chromosomics, Inc. These authors acknowledge a potential conflict of interest and attest that the work contained in this report is free of any bias that might be associated with the commercial goals of the company. The other authors declare no competing interests.

Additional information

Supplementary information The online version contains supplementary material available at https://doi.org/10.1038/s42003-025-07827-0.

Correspondence and requests for materials should be addressed to Shunsuke Kita, Yoshimasa Takahashi or Katsumi Maenaka.

Peer review information *Communications Biology* thanks Scott McConnell and the other, anonymous, reviewer(s) for their contribution to the peer review of this work. Primary Handling Editors: Theam Soon Lim and Laura Rodríguez Pérez.

---

[1]Laboratory of Biomolecular Science, and Center for Research and Education on Drug Discovery, Faculty of Pharmaceutical Sciences, Hokkaido University, Sapporo, Japan. [2]Research Center for Drug and Vaccine Development, National Institute of Infectious Diseases, Tokyo, Japan. [3]Laboratory for Drug Discovery & Disease Research, Shionogi & Co., Ltd., Osaka, Japan. [4]Division of Molecular Pathobiology, International Institute for Zoonosis Control, Hokkaido University, Sapporo, Japan. [5]Institute for Vaccine Research and Development (HU-IVReD), Hokkaido University, Sapporo, Japan. [6]Laboratory of Medical Virology, Institute for Life and Medical Sciences, Kyoto University, Kyoto, Japan. [7]Department of Pathology, National Institute of Infectious Diseases, Tokyo, Japan. [8]Chromosome Engineering Research Center, Tottori University, Tottori, Japan. [9]Department of Chromosome Biomedical Engineering, School of Life Science, Faculty of Medicine, Tottori University, Tottori, Japan. [10]Trans Chromosomics Inc., Yonago, Japan. [11]One Health Research Center, Hokkaido University, Sapporo, Japan. [12]International Collaboration Unit, International Institute for Zoonosis Control, Hokkaido University, Sapporo, Japan. [13]Global Virus Network, Baltimore, MD, USA. [14]CREST, Japan Science and Technology Agency, Kawaguchi, Japan. [15]Kyoto University Immunomonitoring Center, Kyoto University, Kyoto, Japan. [16]Division of Pathogen Structure, International Institute for Zoonosis Control, Hokkaido University, Sapporo, Japan. [17]Global Station for Biosurfaces and Drug Discovery, Hokkaido University, Sapporo, Japan. [18]Faculty of Pharmaceutical Sciences, Kyushu University, Fukuoka, Japan. ✉e-mail: kita@pharm.hokudai.ac.jp; ytakahas@niid.go.jp; maenaka@pharm.hokudai.ac.jp